

Supporting Information

Harvesting Resonantly-Trapped Light for Small Molecule Oxidation Reactions at the Au/ α -Fe₂O₃ Interface

Joshua P. McClure¹, Kyle N. Grew¹, David R. Baker¹, Eric Gobrogge¹, Naresh Das¹ and Deryn
Chu¹

¹U.S. Army Research Laboratory, Adelphi, MD, 2800 Powder Mill Road, Adelphi, MD 20783,
U.S.A.

Contents:

Theoretical: DDA Simulations

Figure S1. CWL and AM1.5G experimental apparatuses

Figure S2. Multi-layered Au/ α -Fe₂O₃ electrode schematics

Figure S3. Diameter distributions and AFM Images for the α -Fe₂O₃/Au photo-electrodes

Figure S4. Representative Raman spectra and Fe2p high-resolution narrow scans

Table S1. XPS peak fitting information for O1s and Au4f high-resolution narrow scans

Figure S5. Representative photo-potential baseline processing

Figure S6. Comparison of the photo-potential for the different Au/ α -Fe₂O₃ electrodes

Figure S7. Representative chronoamperometry baseline processing

Figure S8. Comparison of the chronoamperometry for the different Au/ α -Fe₂O₃ electrodes

Figure S9. Light-chopping CWL experiments in 0.1M KOH

Figure S10. Near-field cross-sections for $\lambda = 532$ and 785 nm excitations

References

Discrete Dipole Approximation Simulations

Electromagnetic scattering simulations have been performed using DDScat, which implements the discrete dipole approximation (DDA) methodology for solving Maxwell's equations.¹⁻³ DDA numerically solves Maxwell's equations for monochromatic plane wave radiation. The target geometry is discretized as an array of (polarizable) point dipoles, which are represented as spheres and assembled onto a regular cubic lattice.¹ It is applicable to both finite and periodic target, subject to the conditions that dipole separation are small relative to the feature lengths within the target and the wavelength of the electromagnetic radiation.¹⁻² Electromagnetic scattering is calculated when the dipoles are treated as polarizable. The standard Clausius-Mossotti relationship is used within DDScat.¹ Accordingly, the dipole polarizability is a function of the effective size, number density, and relative dielectric constant. Details on this treatment may be found elsewhere.¹

DDA is applicable to the simulation of both near- and far-field electromagnetic scattering phenomena. Far-field scattering properties, such as the absorption, scattering, and extinction cross-sections as well as the generalized absorption, transmission, and reflection coefficients may directly be simulated using this approach.¹ The fraction of the incident power that is absorbed, reflected, and transmitted are used to calculate the absorptance, transmittance, and reflectance values. As detailed by Draine and Flatau, these properties may be directly calculated from the relative Stokes vector components within the (simulated) far-field scattering matrix.² The near-field electromagnetic scattering may also be calculated from the simulations, which takes the

form of the relative (local) electric field intensity, $\left| \frac{E(x,y,z)}{E_o} \right|_2$. The relative electric field intensity is a product of both the incident electromagnetic field as well as that which results from the

polarization (coherent oscillations) of all other dipoles. Flatau and Draine have published comprehensive discussions on the associated theory and methods, which is not repeated here³

Within the current study, doubly periodic targets (plane of the Fe₂O₃ layer) subject to plane wave radiation at a prescribed (visible) wavelength were simulated. Inputs were oriented such that the incident electromagnetic radiation was normal to the periodic plane. The dipoles were scaled such that their effective diameter was less than 5 nm - so as to meet the density and sizing requirement of the DDA method across the visible spectrum. All targets were numerically generated and verified in Matlab. Both the near-field and far-field electromagnetic scattering characteristics were calculated with the DDA methodology for this study.

To provide a more systematic and quantitative measure of the influence of the structure materials and geometry on the near-field scattering, a volume-normalized near-field enhancement, $\rho(\lambda, \varphi)$, is considered within the current study. This enables us to numerically track and probe the near-field enhancements as a function of the wavelength λ , and phase (or region), φ .

$$\rho(\lambda, \varphi) = \frac{1}{V_\varphi} \int_V \left| \frac{E}{E_0} \right|^2 dV_\varphi$$

Figure S1

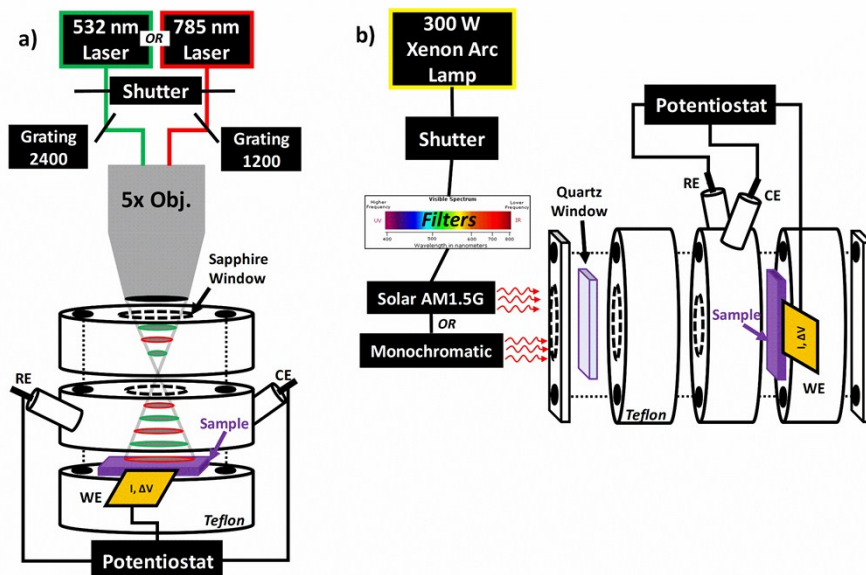


Figure S1. Three-electrode cell schematics of a) three-piece Teflon cell used in the continuous wave laser (CWL) experiments with a port for attachment to the $5\times$ objective from either a $\lambda = 532$ or 785 nm source and b) five-piece Teflon cell used in the solar-simulated (AM1.5G) experiments. Note: Both cell configurations are fabricated for front-side illumination with built-in ports for the reference (Ag/AgCl Sat. KCl), counter (Pt Coil) and working electrodes, as well as additional port for head-space purging with N_2 .

Figure S2

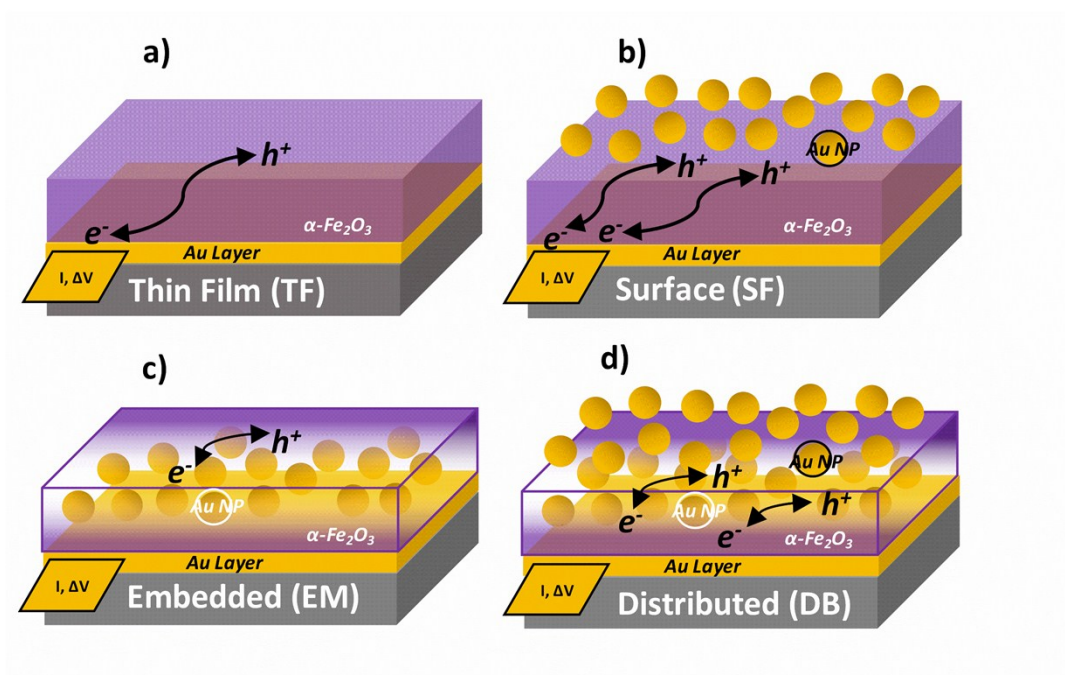


Figure S2. Multi-layered Au/α-Fe₂O₃ electrode schematics for the a) thin film (TF) b) surface (SF) c) embedded (EM) and d) distributed (DB) configurations.

Figure S3

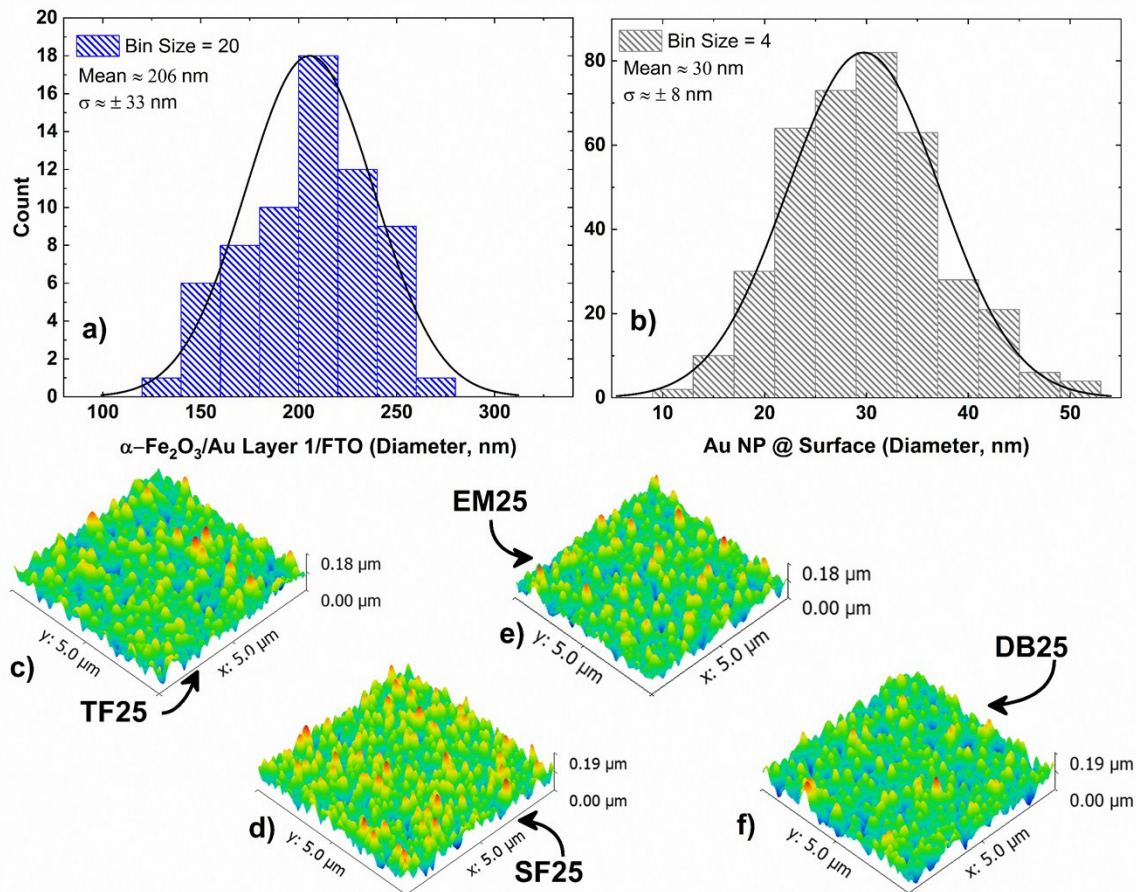


Figure S3. Diameter distributions for a) α -Fe₂O₃/Au Layer 1/FTO substrate and b) the surface Au NPs atop the α -Fe₂O₃ layer. Atomic force microscopy (AFM) images for TF, SF, EM and DB configurations (c-f) with a nominal 25 nm α -Fe₂O₃ thickness and a measured 25 μ m² area.

Figure S4

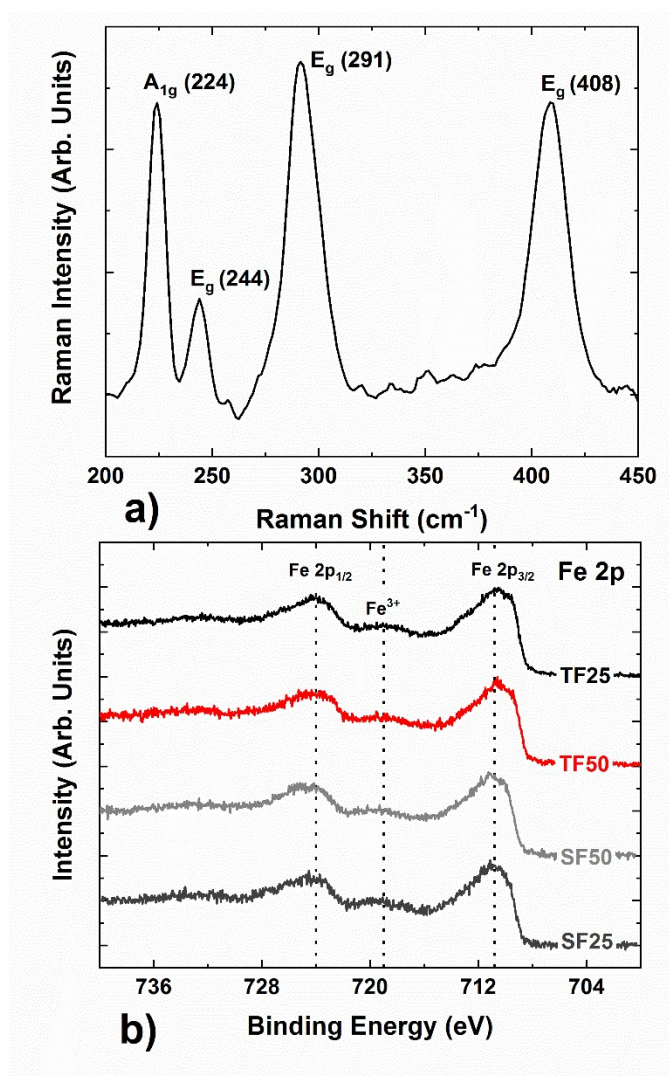


Figure S4. A representative a) Raman spectra of the surface configured Au/ α -Fe₂O₃ electrode and b) Comparison of the XPS high-resolution Fe2p region for different thin film (TF) and surface (SF) configurations with nominal 25 and 50 nm α -Fe₂O₃ thicknesses.

Table S1

	TF25		TF50		TF75	
	O1s Peak 1	O1s Peak 2	O1s Peak 1	O1s Peak 2	O1s Peak 1	O1s Peak 2
Position (eV)	529.76	530.88	529.67	530.93	529.96	530.85
FWHM	1.00	3.09	1.06	2.54	0.96	2.78
Area (%)	62.47	37.53	69.66	30.34	70.96	29.04
Std. Dev. (%)	0.90	0.90	2.55	2.55	0.48	0.48
	SF25		SF50		SF75	
	O1s Peak 1	O1s Peak 2	O1s Peak 1	O1s Peak 2	O1s Peak 1	O1s Peak 2
Position (eV)	530.08	531.43	530.22	531.47	530.02	531.22
FWHM	1.07	2.82	1.05	2.70	0.96	2.62
Area (%)	53.11	46.89	58.34	41.66	71.01	28.99
Std. Dev. (%)	2.91	2.91	2.94	2.94	1.56	1.56
	SF25		SF50		SF75	
	Au4f _{7/2}	Au4f _{5/2}	Au4f _{7/2}	Au4f _{5/2}	Au4f _{7/2}	Au4f _{5/2}
Position (eV)	83.99	87.66	84.08	87.75	84.11	87.79
FWHM	0.87	0.86	0.87	0.89	0.78	0.80
Area (%)	50.69	49.31	50.37	49.63	50.28	49.72
Std. Dev. (%)	0.14	0.14	0.15	0.15	0.09	0.09

Table S1. X-ray photo-electron spectroscopy high-resolution peak fitting results for the O1s and Au 4f peak regions. Note: FWHM and Std. Dev. (%) refer to the full-width at half-maximum and standard deviation percentage, respectively.

Figure S5

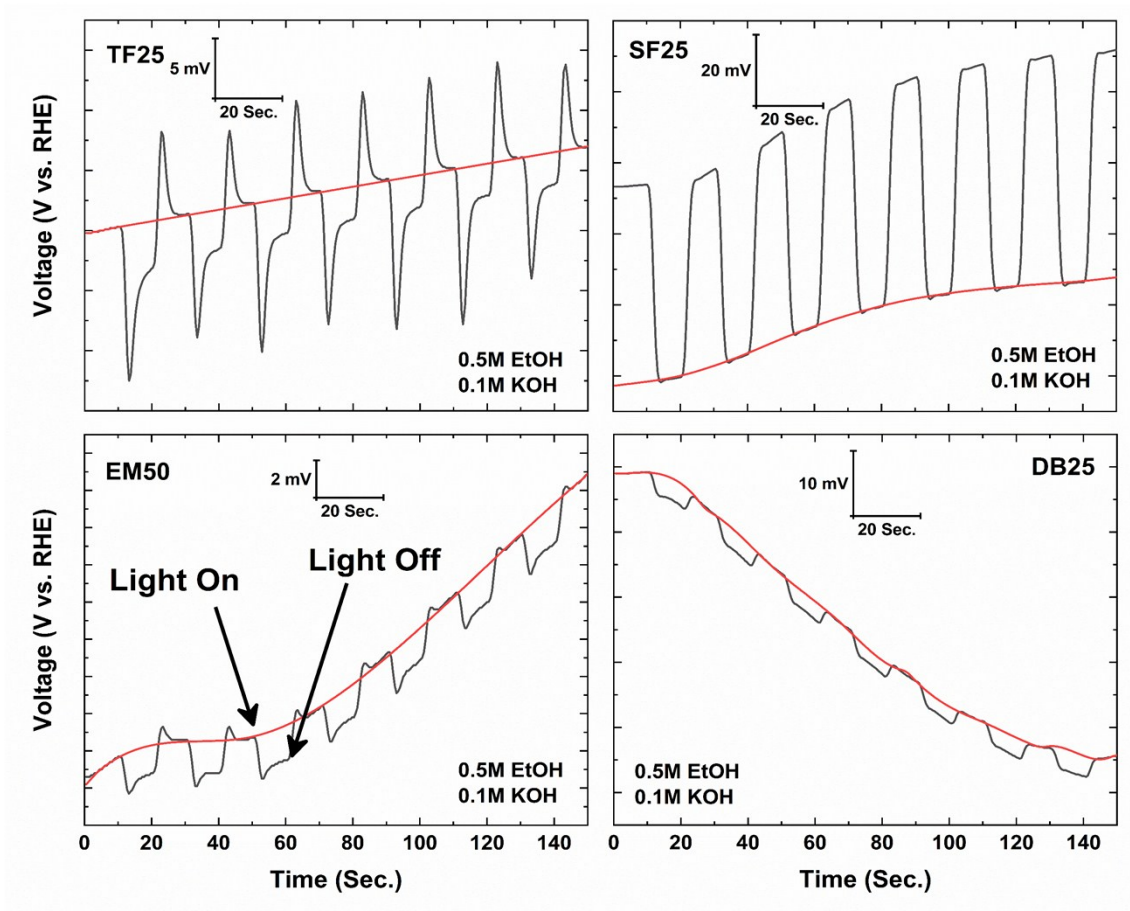


Figure S5. Representative baseline processing for photo-potential for select samples. The baseline subtractions allow for an easy comparison of the photo-response of the open-circuit voltage as shown in Fig. S6.

Figure S6

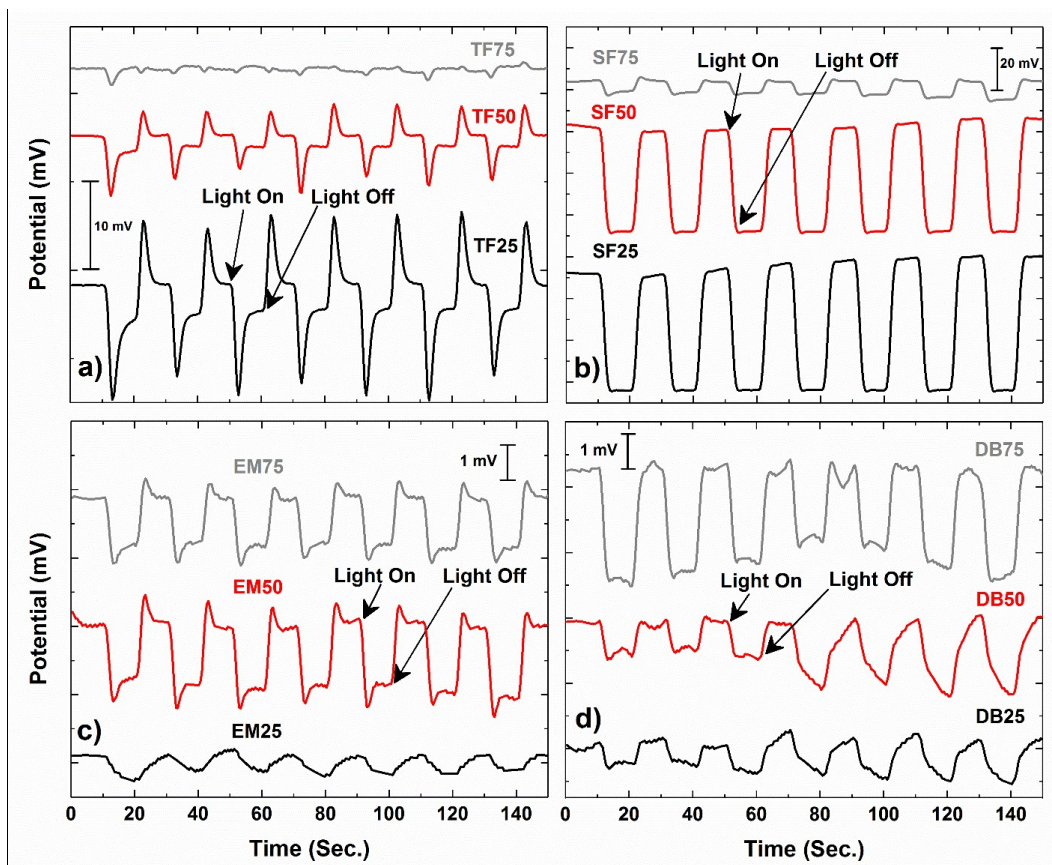


Figure S6. Light-chopping solar-simulated (AM1.5G) open-circuit potential experiments performed for twelve different thin film (TF), surface (SF), embedded (EM) and distributed (DB) configurations in 0.1M KOH and 0.5M EtOH. (Note: SF25 refers to a nominal 25 nm α -Fe₂O₃ film thickness)

Figure S7

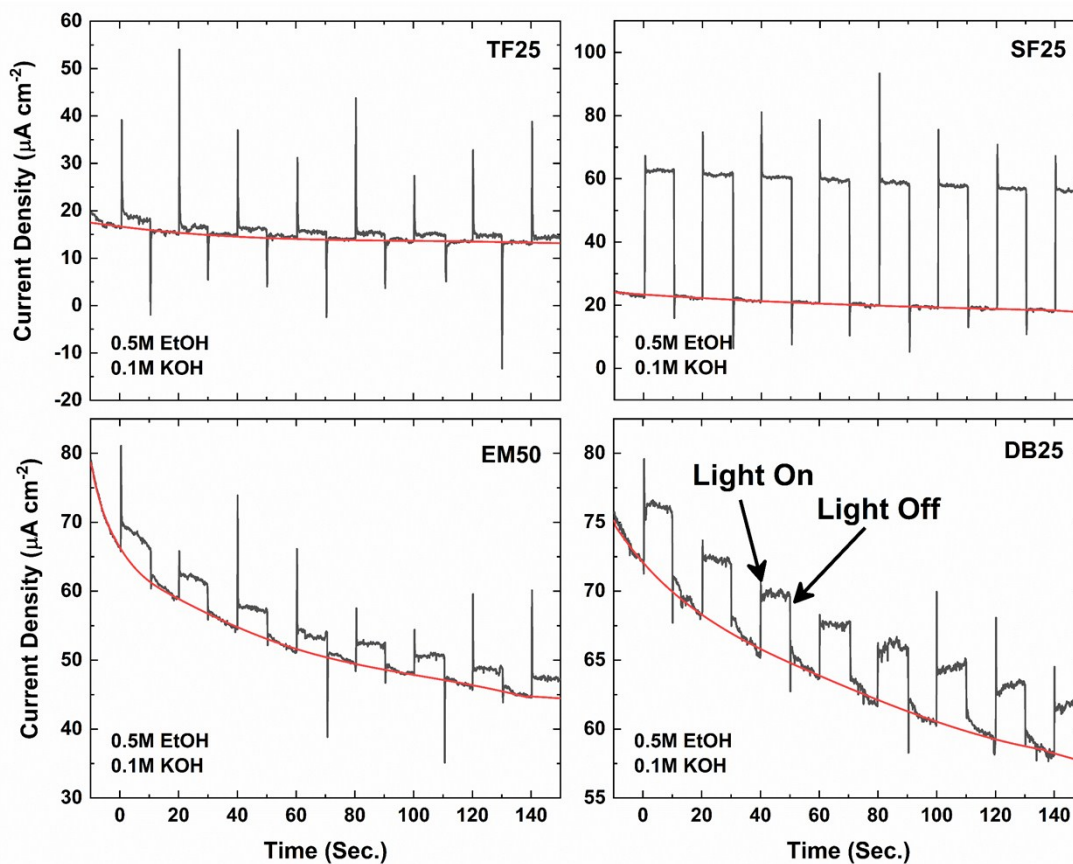


Figure S7. Representative baseline processing for chronoamperometry measurements for select samples. The baseline subtractions allow for an easy comparison of the photo-response of the chronoamperometry as shown in Fig. S8.

Figure S8

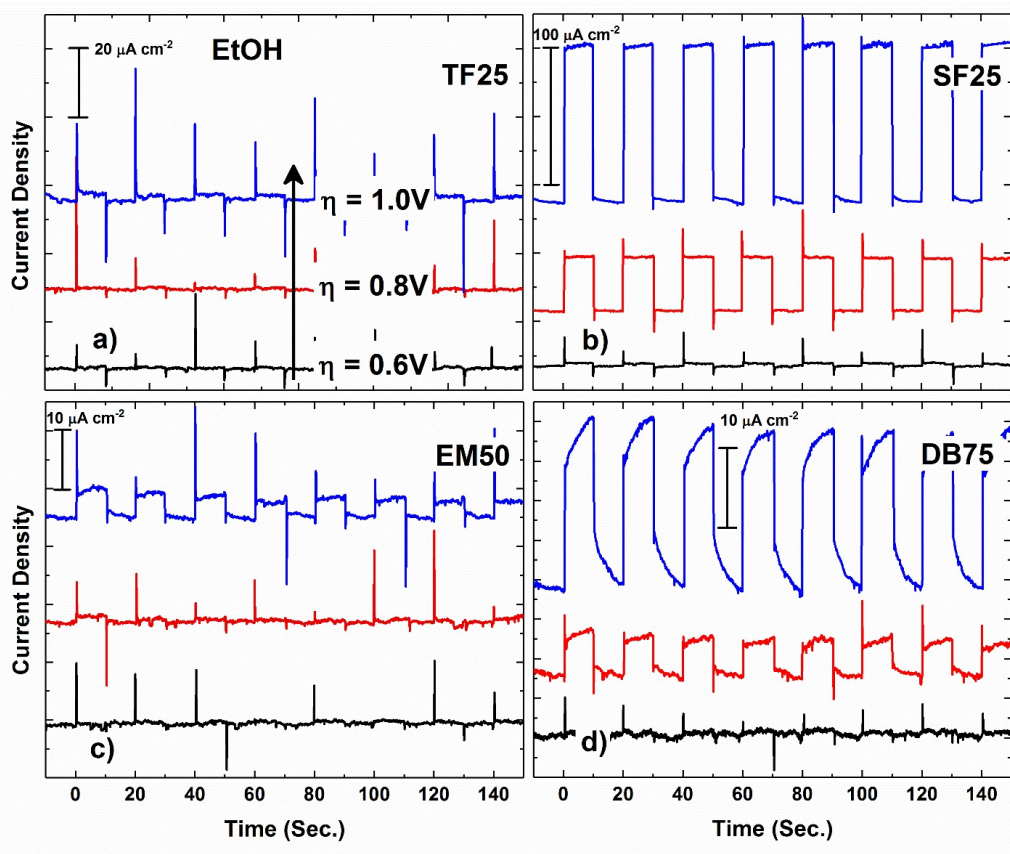


Figure S8. Light-chopping solar-simulated (AM1.5G) chronoamperometry experiments performed for the best performing thin film (TF), surface (SF), embedded (EM) and distributed (DB) configurations in 0.1M KOH and 0.5M EtOH. The light-chopping is shown for three different overpotentials (η). (Note: SF25 refers to a nominal 25 nm α -Fe₂O₃ film thickness)

Figure S9

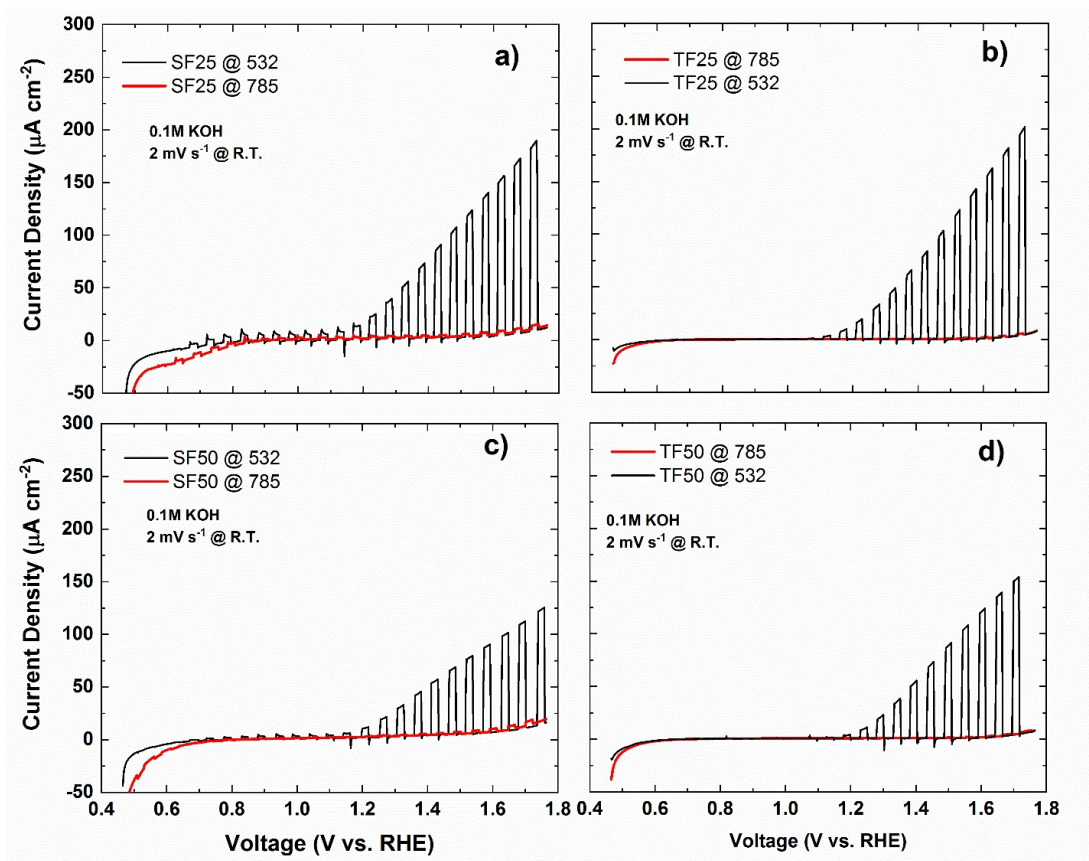


Figure S9. Light-chopping continuous-wave (CWL) experiments shown for select thin film (TF) and surface (SF) configurations in 0.1M KOH only media. All experiments performed at room temperature (R.T.) for $\lambda = 532$ and 785 nm above-below $\alpha\text{-Fe}_2\text{O}_3$ band-gap excitations, respectively. (Note: SF25 refers to a nominal 25 and 50 nm $\alpha\text{-Fe}_2\text{O}_3$ film thicknesses)

Figure S10

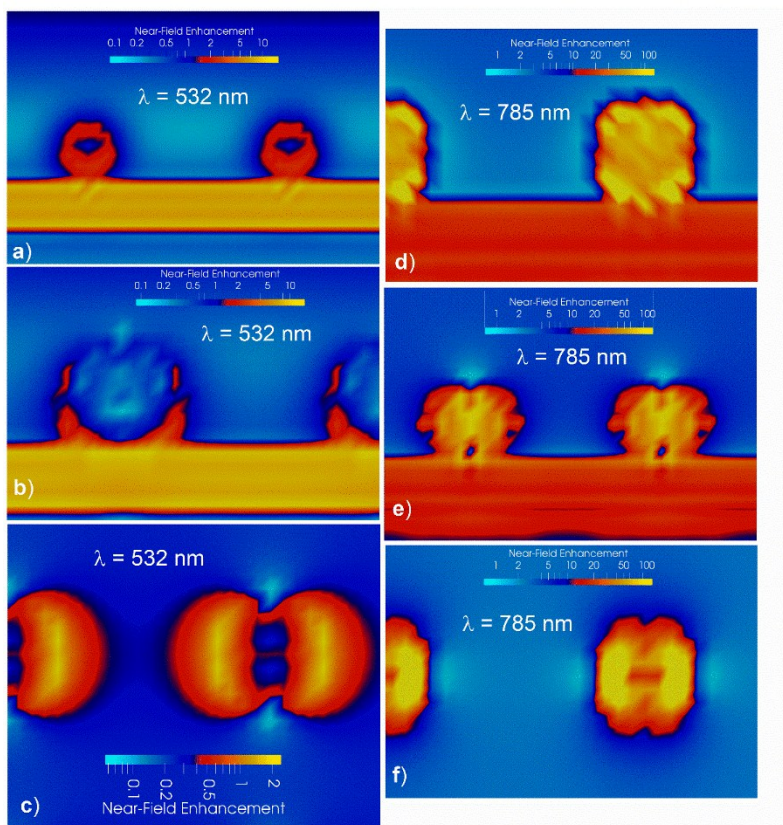


Figure S10. Cross-sections shown for the SF configuration with a 25 nm $\alpha\text{-Fe}_2\text{O}_3$ thick layer. X-Slice (a-b), Y-slice (c-d) and Z-slice (e-f). The near-field cross-sections are shown for $\lambda = 532$ (above) and 785 nm (below) $\alpha\text{-Fe}_2\text{O}_3$ band-gap excitations, respectively.

References

1. Draine, B. T.; Flatau, P. J., Discrete-Dipole Approximation For Scattering Calculations. *J. Opt. Soc. Am. A* **1994**, *11* (4), 1491-1499.
2. Draine, B. T.; Flatau, P. J., Discrete-dipole approximation for periodic targets: theory and tests. *J. Opt. Soc. Am. A* **2008**, *25* (11), 2693-2703.
3. Flatau, P. J.; Draine, B. T., Fast near field calculations in the discrete dipole approximation for regular rectilinear grids. *Opt. Express* **2012**, *20* (2), 1247-1252.